Journal of The Electrochemical Society, 2025 **172** 037503
1945-7111/2025/172(3)/037503/12/$40.00 © 2025 The Electrochemical Society ("ECS"). Published on behalf of ECS by IOP Publishing Limited.

Machine Learning Regression for Assessing Sensing Performance and Anticancer Potential of Oolong Tea-Derived Silver Nanoparticles

Esra Sert,[1] Ferdane Danışman Kalındemirtaş,[2] Emir Ersel Karakuş,[3] Ayşe Erol,[4] Fatih Özbaş,[5] Tarık Küçükdeniz,[6] and Selcan Karakuş[7,8,z]

[1]*Department of Hematology, Istanbul Faculty of Medicine, Istanbul University, 34390 Istanbul, Türkiye*
[2]*Department of Physiology, Faculty of Medicine, Erzincan Binali Yildirim University, Erzincan, Türkiye*
[3]*Private Nazmi Arıkan Science School, 34906 Istanbul, Türkiye*
[4]*Department of Medical Biology, Istanbul Faculty of Medicine, Istanbul University, Istanbul, Türkiye*
[5]*Department of Restoration and Conservation of Cultural Assets, Faculty of Arts, Design and Architecture, Fatih Sultan Mehmet Vakif University, Istanbul, 34015, Türkiye*
[6]*Department of Industrial Engineering, Faculty of Engineering, Istanbul University-Cerrahpaşa, Istanbul 34320, Türkiye*
[7]*Department of Chemistry, Faculty of Engineering, Istanbul University-Cerrahpaşa, 34320 Istanbul, Türkiye*
[8]*Health Biotechnology Joint Research and Application Center of Excellence, 34220 Esenler, Istanbul, Türkiye*

In this study, machine learning (ML) algorithms were employed to predict analyte concentrations using sensing results and evaluate the anticancer effects of nanostructures. Multifunctional oolong tea extract-mediated silver nanoparticles (OTE-Ag NPs) were synthesized via a photo/ultrasound method and utilized in various applications, including a smartphone-based H_2O_2 sensor and electrochemical sensors for urea and fructose. Key features were extracted from electrochemical results, and feature importance analysis was used to select the most predictive features. The artificial neural network (ANN) model provided accurate predictions, particularly strong for urea ($R^2 = 0.8575$, RMSE = 0.4266, MAE = 0.3380). The study revealed the selective toxicity of OTE-Ag NPs to MCF-7 breast cancer cells through analyses of cytotoxicity, apoptosis, cell cycle phases, and CD44 surface marker expression using Annexin V/PI dye and flow cytometry. Experimental results demonstrated that OTE-Ag NPs suppressed MCF-7 cell proliferation while exhibiting lower cytotoxicity in normal HUVEC cells (46% cell death). OTE-Ag NPs arrested MCF-7 cells in the G2/M phase, induced apoptosis, and reduced CD44 expression, suggesting metastasis suppression. The CD44+/CD24- ratio decreased from 84.79% in control MCF-7 cells to 47.7% in OTE-Ag NP-treated cells. Overall, OTE-Ag NPs significantly inhibited MCF-7 cell proliferation through the apoptotic pathway by regulating the cell cycle in the G2/M phase.
 [DOI: 10.1149/1945-7111/adb90f]

Manuscript submitted November 25, 2024; revised manuscript received February 3, 2025. Published March 4, 2025.

Oolong tea (OT), derived from Camellia sinensis leaves, has demonstrated antioxidant, anticancer, anti-inflammatory, and activity in a variety of in vivo and in vitro studies. Despite these promising results, there has been limited research on the health-promoting properties of OT and its constituents. Several studies have reported the potential efficacy of possible effectiveness of OT bioactives, investigating their functions as potentially useful chemotherapy agents, cardioprotective effects in hypoxic environments, treatment of allergic diseases, possible prebiotic processes, enhancement of blood lipid status in humans, and efficacy as an oral hypoglycemic agent for type 2 diabetes. Additionally, OT has shown potential in reducing the risk of obesity.[1] OT exhibits inhibitory effects on breast cancer cell development, proliferation, and carcinogenesis, presenting high potential as a chemopreventive therapy. Notably, substantial research has been conducted on its anticancer activities owing to the lower occurrence of breast cancer and a higher proportion of green tea consumption in the Asian population.[2] Approximately one-fifth of cancer patients worldwide suffer from breast cancer, making it the most common and deadliest malignant disease among women globally.[3] Although anticancer medications used to treat breast cancer are effective against malignant cells, they can also harm normal cells at a similar rate, leading to numerous undesirable side effects, including systemic toxicity. Conventional formulations of therapeutic agents often have poorer penetration into cancer cells due to reduced dispersion and faster elimination. Green nanoparticles (NPs) play a vital role in the controlled administration of various chemotherapeutic therapies. By employing NPs to deliver chemotherapy treatments, it is possible to avoid side effects, such as toxicity and dosage dumping, while achieving the desired medication concentration in a specified location.[4–7] The market for more effective, tailored cancer treatments that can improve treatment efficacy while lowering side effects is severely lacking, and this work fills that gap. The goal of this research is to greatly enhance cancer treatment delivery systems by using green nano-drugs. OT has been extensively studied for its anticancer properties; however, there is relatively little research on the association between green materials and breast cancer.[2] With the growing need for advanced cancer treatments in patients with chemo resistant tumor populations and significant tumor loads, nanodrug delivery systems have become crucial. In response to this need, numerous nanodrug delivery systems have become essential components of anticancer treatment strategies. Ongoing research in the fields of cancer and nanotechnology has yielded several solutions to major issues in new therapeutic methods. The distinct colloidal behaviors of various NP types, coupled with various targeting techniques, have enabled the optimization of combination cancer treatments in ways never before possible.[8]

Cancer stem cells (CSCs) were initially identified in hematological malignancies and possess the capacity to self-renew and specialization into multiple tumor cell lineages. Representing a small subset of tumor cells, CSCs are distinguished by their capacity to generate daughter tumor cells, undergo self-renewal, and maintain key tumor characteristics. Additionally, CSCs play an essential role in tumor metastasis and resistance to radiation and chemotherapy.[9] Human breast cancer CSCs typically exhibit the CD44+/CD24 phenotype.[10] Cancer researchers are actively exploring strategies to prevent metastasis and treat cancer post-metastasis. Like normal stem cells, CSCs can differentiate into various cancer cells, contributing to tumor formation and growth [10]. In this study, we observed a reduction in CD44 expression—a factor implicated in metastasis—upon treatment with green OTE-Ag NPs.

NPs-based sensors have recently received a lot of interest due to their great sensitivity and selectivity, making them useful in domains like medical imaging, monitoring the environment, food safety, and electrochemical sensors.[11–13] For instance, Mishra et al. demonstrated the green synthesis of *Ocimum sanctum*-mediated Ag NPs for hydrogen peroxide detection,[14] while Mujeeb Ur Rahman et al.

[z]E-mail: selcan@iuc.edu.tr

developed a colorimetric sensor for selective manganese detection using green-synthesized Ag NPs derived from *Withania somnifera*.[15,16] Additionally, Ali et al. synthesized orange peel extract-Au NPs and CuO-based nonenzymatic sensors for saliva glucose monitoring.[16] Chaudhary et al. introduced *Nose-on-Chip* nanobiosensors for the early detection of lung cancer breath biomarkers, highlighting the potential of nanotechnology in non-invasive cancer diagnostics.[17] These studies underscore the significant role of green-synthesized NPs in advancing sensing technologies for biomedical applications.

Sensors based on carbon, metal oxide, and metal NPs, especially, have led to revolutionary advances in advanced sensor technology due to their distinct features that improve detecting methods. Furthermore, integrating machine learning (ML) algorithms with sensor technology has improved data processing, pattern identification, and decision-making processes, allowing for the creation of intelligent and more efficient sensing platforms. Automated methods for data analysis such as artificial intelligent (AI) support decision-making without the need for explicit guidance.[18–21] One of the most popular ML techniques for identifying intricate correlations is the usage of artificial neural networks (ANN). As a unique strategy for electrochemical detection platforms spanning many applications, the use of ANN-based ML algorithms is currently being studied in biomedical applications.[22,23] A novel approach to the intelligent analysis of nanostructures-based sensors and novel strategies for incorporating electrochemical nanostructures-based sensors into smart devices are offered by ML techniques.

The novelty of this study lies in its innovative approach, which includes the synthesis of multifunctional OTE-Ag NPs through a novel dual photo/ultrasound method, their comprehensive characterization, and their application in ML-based sensing. Several techniques—transmission electron microscopy (TEM), Fourier-transform infrared spectroscopy (FTIR), X-ray diffraction (XRD), and scanning electron microscopy with energy-dispersive X-ray spectroscopy (SEM-EDX)—were used to analyze the surface morphology and identify the functional groups of the synthesized OTE-Ag NPs. We investigated their H_2O_2 biosensing and anticancer activities for the first time, revealing exceptional effectiveness against breast cancer cells MCF-7. The prepared OTE-Ag NPs exhibited excellent sensitivity and selectivity for H_2O_2 detection, achieving a low limit of detection (LOD) of 0.102 μM in one minute. Additionally, ML-based electrochemical LODs for the OTE-Ag NPs were determined to be 3.02 μM for urea and 4.86 μM for fructose. Furthermore, the specific toxicity of OTE-Ag NPs towards MCF-7 breast cancer cells was demonstrated by cytotoxicity, apoptosis, cell cycle arrest, and expression of the CD44 surface marker.

Material and Method

Chemicals.—OT (Camellia sinensis, Huang Guanyin) was collected in April 2022 from Wuyishan, China, (at 27 °C and the humidity was 53 ± 1%). Freshly selected leaves underwent a three-hour withering phase in accordance with OT's processing procedure. Subsequently, the temperature was maintained at 25 °C, and the grinding motion was performed at a constant rate of 25 cycles per minute. Whatman® qualitative filter paper 1, NaOH, silver nitrate ($AgNO_3$, purity⩾99.0%), MTT test kit for cell proliferation, DMSO, FBS, DMEM, streptomycin, penicillin, Annexin-V/PI, glucose, lactose, maltose, testosterone, dopamine, and progesterone were purchased from Sigma Aldrich Company. Sterile syringe filter (0.45 μm), ethanol and hydrogen peroxide (H_2O_2) were purchased from Merck Company.

The American Type Culture Collection, known as ATCC is the source of the MCF-7 and HUVEC cells. Moreover, no further purification was required because all compounds were of analytical grade.

The process of cytotoxicity.—In this study, we used human umbilical vein endothelial cells (HUVECs) and the human breast cancer cell line MCF-7. These cells were cultured at 37 °C in an environment that was humidified with 95% O_2 and 5% CO_2 utilizing DMEM treated with 10% FBS and penicillin-streptomycin. A total of 10^4 cells were planted into each well of a 96-well plate. Then, the synthesised OTE and OTE-Ag NPs were directly added to the wells at 1:1, 1:2, 1:4 and 1:8 dilutions and left to incubate for 48 h. After a 48 h period, each well contained 10 μl of MTT (5 mg ml^{-1}), and the cells were incubated for an additional 4 h. At 570 nm, the density of light was measured with an ELISA reader instrument. The absorbance of the test and control wells was compared to assess the cell viability, which was expressed as a percentage.

The process of apoptosis.—To assess apoptosis using the Annexin V/PI method, 5 μl of Annexin V-FITC, 2.5 μl of PI were introduced to prepared cells, after which there was a 10 min dark incubation period. A flow cytometer (Navios 3L10, Beckman Coulter) was subsequently utilized to assess the cells, and 400 μl of annexin binding buffer were applied.

MCF-7 cells treated with OTE-Ag NPs were stained with annexin V/PI. This made it possible for a four-quadrant histogram to show the differentiation of necrotic cells, live, early apoptotic, and late apoptotic cells. Comparing the OTE-Ag NP-treated MCF-7 cell line with the control group (MCF-7 cell line), the experimental results revealed an acceleration in the proportion of living cells and an accelerated proportion of early and late apoptotic cells. A Beckman Coulter Navios flow cytometry device was used for this analysis, with parameters adjusted to create a template suitable for apoptosis. Data were recorded using Kaluza software. Necrotic cells exhibit compromised membranes, facilitating the penetration of Annexin V throughout the entire plasma membrane, and enabling their staining. Furthermore, co-treatment with propidium iodide (PI) aids in distinguishing apoptotic cells from necrotic cells.[20]

Cell cycle analysis.—The cells were first collected and centrifuged at 300 × g for five minutes, after which the supernatant was removed. Subsequently, 0.5 ml of PBS was added to resuspend the cells. The suspended cells were then transferred to a tube containing 1.2 ml of pure ethanol, maintained at −20 °C, vigorously agitated, and left to incubate for thirty minutes or overnight for preservation. After centrifugation of the cells for five minutes at 1800 rpm, the supernatant was discarded. One milliliter of PBS is added to the suspended cells. For fifteen minutes, it is incubated at room temperature. At 1800 pm, it is centrifuged for five minutes, and the supernatant is discarded once again. For half an hour, the cells were incubated in a water bath at 37 °C with 100 μl RNase A reagent. A volume of 0.4 ml of FxCycleTM PI Staining solution dye was added to each prepared tube. The samples were then incubated in the dark for 30 min at 2 °C-8 °C. A flow cytometer (Beckman Coulter Navios) was used to instantly analyze the samples. The Kaluza Analysis tool was employed to investigate this, and the findings were recorded.

CD44 and CD24.—The prepared cells were washed with cold phosphate-buffered saline (PBS). After staining with PB-conjugated CD44 antibody (5 μl) (ref: B37789: Immunotech Sas a Beckman Coulter Company 13276) and ECD-conjugated CD24 antibody (5 μl) (ref: B12699: Immunotech Sas a Beckman Coulter Company 13276), they were incubated for 30 min in the dark. Following incubation, the cells were identified immediately on the Beckman Coulter Navios flow cytometry instrument using 0.5 ml of PBS. The CD44 high, CD44 negative, and CD44 low populations in the control group (MCF7 cell line) and the OTE-Ag NPs treated MCF7 cell group were separated using the Beckman Coulter Navios system and recorded using Kaluza software.

The photo/ultrasound-mediated synthesis of OTE-Ag NPs.—The photo/ultrasound-based synthesis of OTE-Ag NPs involves several steps. In our previous research, we thoroughly investigated the extraction process of tea (OTE).[21] To remove dust and

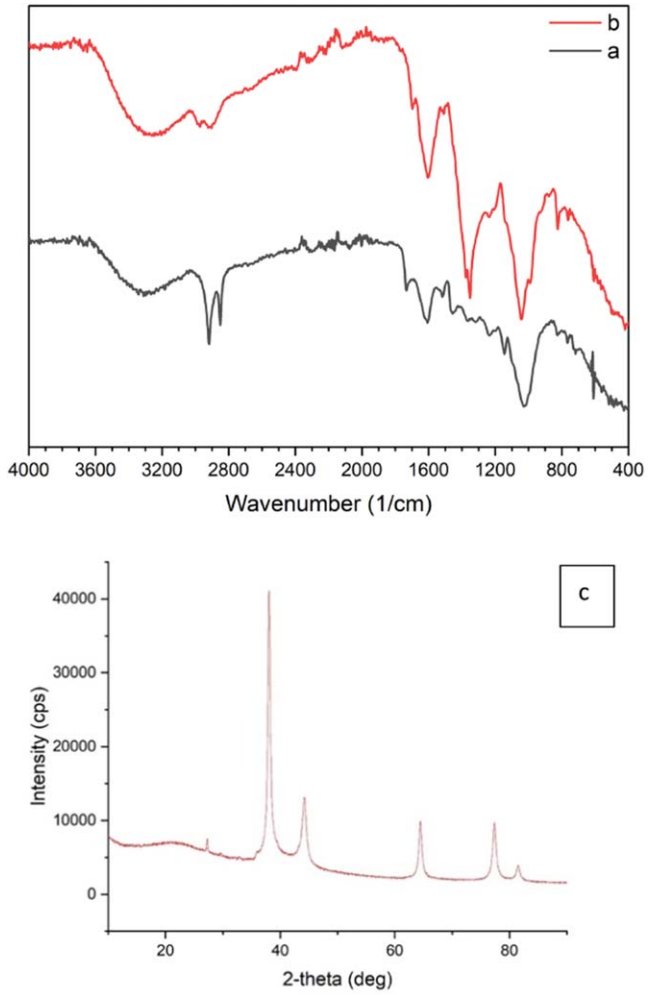

Figure 1. FTIR spectra of (a) OTE and (b) OTE-Ag NPs, and (c) XRD graph of the OTE-Ag NPs.

contaminants, OT was first purified by rinsing it with ultrapure water and then drying it in vacuum for five hours at 50 °C. Subsequently, 250 ml of ultra-pure water was added to 5 g of dried OT, and the mixture was incubated for 5 days at 25 °C in the dark. The resultant OE was kept in sterile containers at 25 °C after filtration using a sterile syringe filter (0.45 μm). The fabrication of the OTE-Ag NPs was achieved through a dual photo/ultrasound process. In particular, 0.1 g of NaOH was dissolved in 125 ml of ultrapure water, and 0.42 g of AgNO3 was dissolved in 250 ml of distilled water. After dropping the NaOH solution into a 50 ml silver solution, the resultant mixture was sonicated for 30 min at room temperature. UV radiation from an LED lamp (UV 395–400 nm) was employed during the sonication process, with the lamp positioned 20 cm away from the sample. Effective reaction conditions were provided by the lamp intensity, which was determined at 3 W with an optical power meter (Newport 1916-C) when combined with a thermopile detector. Finally, a sterile syringe filter (0.45 μm) was employed to carefully filter the resultant OTE-Ag NPs.

Characterization.—Using the Perkin Elmer FTIR spectrophotometer model, Fourier-transformed infrared (FTIR) spectra covering the wavelength range of 4000 to 400 cm^{-1}, the chemical functional groups of the photo/ultrasound produced OTE-Ag NPs were determined. The chemical structure of the produced OTE-Ag NPs was investigated within the range of 2θ from 5° to 90° using X-ray diffraction (XRD, D8 advanced Bruker model) analyses. Transmission electron microscopy (TEM, JEOL JEM-2100 Plus model) was employed at 200 kV to investigate the surface features and particle sizes of the NPs in more detail. With a gold-coating technique at an accelerating voltage of 20 kV, energy-dispersive X-ray spectroscopy (SEM/EDX, Oxford XACT) and scanning electron microscopy (SEM, JEOL JMS-7001F) were employed to evaluate the surface and chemical characteristics of the photo/ultrasound developed OTE-Ag NPs.

Digital colorimetric sensing of H_2O_2 utilizing photo/ultrasound synthesized Ag NPs.—Digital sensor tests were carried out by equally dispersing 50 μl of dual photo/ultrasound synthesized OTE-Ag NPs onto a 10 cm^2 area of a pristine Whatman Filter paper 1. Using an air cannon with a 1.5 mm nozzle diameter, the spray coating technique was used to complete this application. The coated paper was then left to dry at 40 °C. Each applied analyte was dropped onto the nanostructure-coated surface (0.2 ml) and allowed to dry at 40 °C. To detect H_2O_2, all images of surfaces covered in filter paper, whether coated, uncoated, or treated with analyte, were captured using a smartphone device camera (Casper via F20 model; rear camera: 48MP-5MP-2MP-2MP).The sensor parameters (LOD and LOQ) were determined over a wide range from 0.5–100 μM. Different analytes such as urea, glucose, and lactose were used in the selectivity experiments of the digital sensor. The color signals (red-green-blue RGB) were evaluated to test the sensitivity of the sensor. The colors RGB (0, 0, 0) stand for black, RGB (255, 0, 0) for red, RGB (0, 255, 0) for green, and RGB (0, 0, 255) for blue in the digital RGB image color model.

Machine learning-assisted analyte concentration prediction.—In this section, ML techniques are utilized to predict the concentrations of specific analytes using CV data. The initial step in this analytical approach involves a feature engineering process, which is crucial for transforming raw electrochemical signals into a structured dataset amenable to ML analysis.

The feature engineering process was initially commenced to extract relevant features from the raw CV data. This process was aimed at converting the electrochemical data into a set of measurable attributes that reflected the underlying dynamics of the chemical reactions. Various aspects of the CV signal, such as charge, peak potentials, current statistics (mean, median, and standard deviation), and higher-order derivatives were systematically computed.

Following feature extraction, the relationship between each feature and the analyte concentration was quantitatively assessed by calculating their correlation coefficients. This step was crucial to identify features that displayed a significant linear relationship with the concentration, either positive or negative. To further refine the feature set, a feature importance analysis was conducted using a preliminary ML model. This analysis was instrumental in identifying the most predictive features, with those exhibiting an importance factor above 0.8 being selected for subsequent modeling. This threshold was established to ensure that only the most relevant features that contributed significantly to prediction accuracy were retained.

With these selected features, the development of predictive models was then carried out using two algorithms: Linear Regression, and ANN. The selection of these algorithms was motivated by their diverse learning mechanisms, ranging from simple linear approaches to more complex neural network methods capable of capturing the nonlinear relationships and interactions between features.

A leave-one-out cross-validation strategy was employed to evaluate and compare the performance of these models robustly, a leave-one-out cross-validation (LOOCV) strategy was employed. This approach involves using a single observation from the original sample as validation data, while the remaining observations serve as training data. This process is repeated such that each observation in the sample is used once as the validation data. LOOCV is particularly advantageous for small datasets as it maximizes the

training data used while still allowing for an unbiased evaluation of the model performance.

The performance of each model was assessed based on several statistical metrics including Root Mean Squared Error (RMSE) (Eq. 1), Mean Absolute Error (MAE) (Eq. 2), and the coefficient of determination (R^2) (Eq. 3).

$$\text{RMSE} = \sqrt{\frac{1}{n}\sum_{i=1}^{n}(y_i - \hat{y}_i)^2} \quad [1]$$

$$\text{MAE} = \frac{1}{n}\sum_{i=1}^{n}|y_i - \hat{y}_i| \quad [2]$$

$$R^2 = 1 - \frac{\sum_{i=1}^{n}(y_i - \hat{y}_i)^2}{\sum_{i=1}^{n}(y_i - \bar{y})^2} \quad [3]$$

These metrics provide insights into the accuracy and predictive power of the models, facilitating an objective comparison across the different algorithms.

Results and Discussion

Characterization of photo/ultrasound synthesized OTE-Ag NPs.—The chemical functional groups, crystalline characteristics and phase composition of the photo/ultrasound synthesized OTE-Ag NPs were determined through the identification of changes in the chemical and crystal structures of OTE-Ag NPs using FTIR and XRD techniques. The detection and confirmation of the distinct structural phases inside the Ag NPs under study is important for an in-depth comprehension of their characteristics and potential applications. In this study, the FTIR technique was utilized to acces chemical functional groups of the OTE-Ag NPs. The FTIR graphs of the OE and OTE-Ag NPs were shown in Figs. 1a and 1b and Table I. Figure 1a displays the distinctive FTIR peaks of the OTE.

Furthermore, the FTIR results of the OE reported in the literature reveal the same functional groups and demonstrate comparable stretching and bending vibrations.[22,25] In addition, the FTIR peaks of the OTE-Ag NPs were given in Fig. 1b. When compared to the FTIR spectrum of the OE, the FTIR results clearly indicate the presence of stabilizing and reducing groups on the surface of the OTE-Ag NPs. According to the proposed mechanism for comparable structures reported in the literature, the hydroxyl groups of flavonoids bonded to the Ag^+ ions that existed in the aqueous extract first, after which the Ag ions were reduced to Ag°, developing OTE-Ag NPs.[23,24]

The XRD peak of the OTE-Ag NPs revealed distinct peaks at 2θ values of 38.02° (111), 44.21° (200), 64.40° (220), and 77.27° (311), indicating the presence of the face-centered cubic (fcc) structure characteristic of Ag° (ICDD PDF-2 Card no:00–004–783).[26,27] By applying Scherrer equation (Eq. 4) of measurements to the reflections found in the XRD result, the particle size of the OTE-Ag NPs was calculated.

$$D = \frac{0.9\lambda}{\beta\, Cos\theta} \quad [4]$$

where D is the dimension, β is the peak breadth, θ is the diffraction angle, and λ is the wavelength of the X-ray. By applying Eq. 1, the average particle size of the OTE-Ag NPs was calculated to be ~18 nm.

In Fig. 2, a comprehensive morphological analysis of the photo/ultrasound synthesized OTE-Ag NPs was presented, showcasing a TEM image, SEM micrograph, and SEM with EDX spectrum. Additionally, the experimental results included a total elemental mapping of the OTE-Ag NPs, illustrating the distribution of all elements present. Specific elemental mapping of oxygen (O), potassium (K), sodium (Na), silver (Ag), aluminum (Al), and sulfur (S) within the OTE-Ag NPs was highlighted, providing detailed insight into the elemental composition and spatial arrangement of the OTE-Ag NPs.

The HR-TEM image of the OTE-Ag NPs is shown in Fig. 2a. The photo/ultrasound synthesized OTE-Ag NPs exhibited a smooth and spherical shape, with a particle diameter ranging from 10 to 20 nm. The TEM results unveiled the existence of well-dispersed, spherical-shaped particles without agglomeration, signifying the formation of green OTE-Ag NPs through the interaction of Ag^+ ions with the extract. These observations were consistent with those in the literature.[28] The surface properties of the OTE-Ag NPs were examined through SEM micrographs (Fig. 2b). The presence of scattered spherical-shaped and clustered structures of the formed OTE-Ag NPs was confirmed, aligning with information available in the literature. This aggregated structure was likely a result of dehydration during sample preparation for SEM analysis.[29] The significant absorption peak of Ag at 3 keV, detected in the elemental analysis by EDS data of the OTE-Ag NPs, was attributed to the predominant presence of Ag in the nanostructure (Fig. 2c). The phytochemical agents from the OE that adhered to the surface of the OTE-Ag NPs were identified as the source of the lower values denoted by C and O in the corresponding results. In Figs. 2d and 2e, the total elemental mapping and color mapping for the elements O, K, Na, Ag, Al, and S present in the prepared OTE-Ag NPs were depicted. The elemental mappings of OTE-Ag NPs were presented in Figs. 2d and 2e. All images were detected to contain O, K, Na, Ag, Al, and S elements for the prepared OTE-Ag NPs. From these results, it was evident that the Ag NPs were distributed homogeneously.

Cytotoxicity of the photo/ultrasound synthesized OTE-Ag NPs.—Despite great progress in cancer therapy, cancer remains one of the world's leading causes of death. Natural substances, especially flavones included in human diets, have been shown to have anti-proliferative and apoptosis-promoting effects on cancer cells.[30,31] There has been a lot of research on the use of nanocarriers

Table I. FTIR results of the OTE and OTE-Ag NPs.

FTIR results of the OTE	References	FTIR results of the OTE-Ag NPs OTE-Ag NPs	References
−OH stretching/3290 cm^{-1}	21–23	−OH stretching/3246 cm^{-1}	21
symmetric $-CH_2$ vibration/2900 cm^{-1}	21–23	symmetric $-CH_2$ vibration/2903 cm^{-1}	21
asymmetric $-CH_2$ vibration/2974 cm^{-1}	21–23	asymmetric $-CH_2$ vibration/2972 cm^{-1}	21
N–H vibration or C=O asymmetric vibration of carboxyl group/1600 cm^{-1}	21–23	N–H vibration or C=O asymmetric vibration of carboxyl group/1603 cm^{-1}	21
carbonyl groups in uronic acids/1377 cm^{-1}	21–23	carbonyl groups in uronic acids /1351 cm^{-1}	21
C–O stretching in carboxylic acids /1045 cm^{-1}	21–23	C–O stretching in carboxylic acids /1042 cm^{-1}	21
		metal–oxygen bonds/824 cm^{-1}	23, 24
		Ag–Ag metal bond/487 cm^{-1}	23, 24
		Ag–Ag metal bond/420 cm^{-1}	23, 24

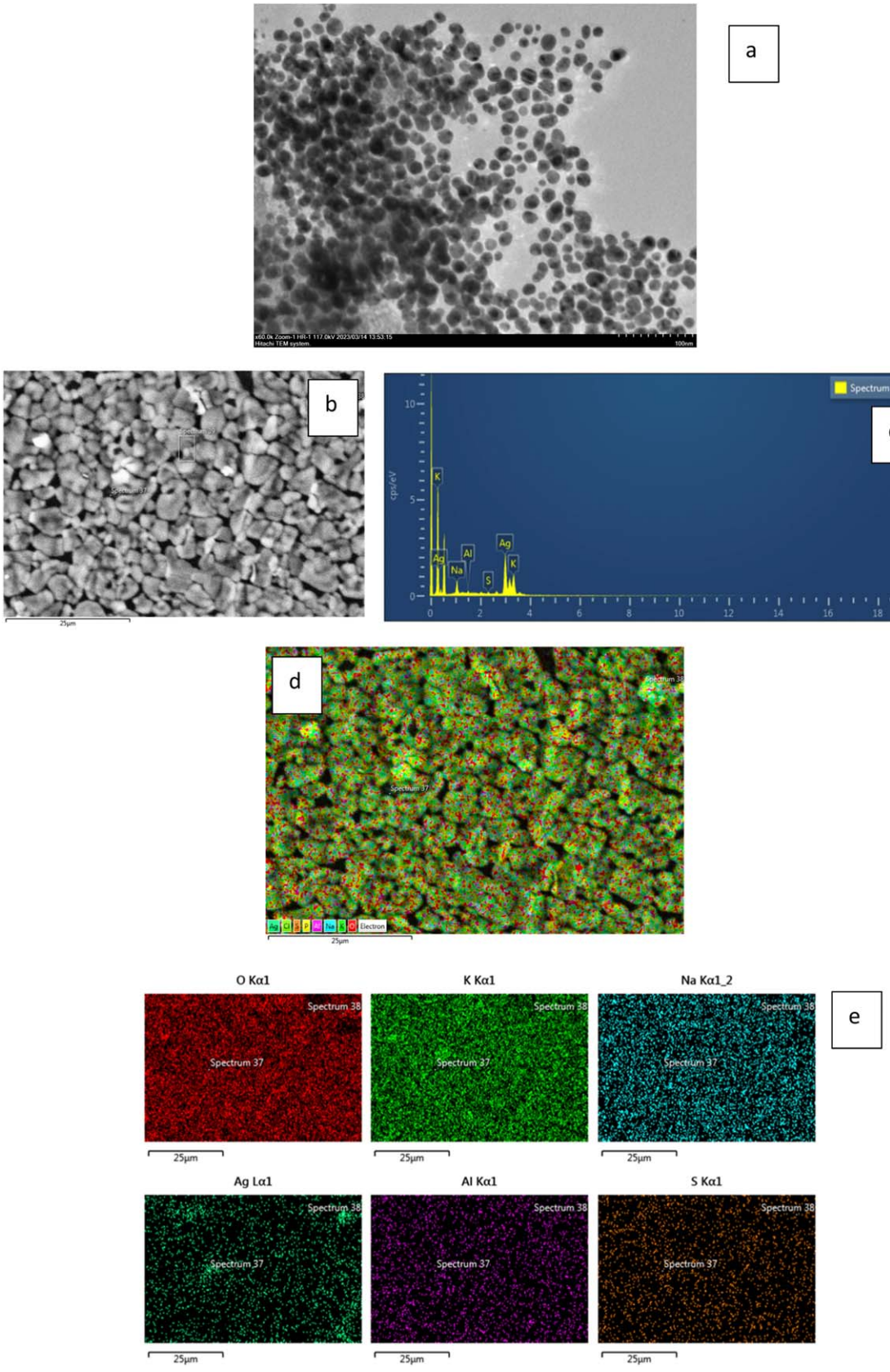

Figure 2. (a) TEM image, (b) SEM micrograph, (c) SEM-EDX spectrum, (d) Total elemental mapping of the photo/ultrasound synthesized OTE-Ag NPs (e) elemental mapping of the O, K, Na, Ag, Al, and S in the OTE-Ag NPs.

containing medications or bioactive substances that exist naturally that inhibit the growth of cancer cells. It has been reported that plant-mediated metallic nanoparticles increase cytotoxicity and apoptotic activity.[32,33] In another study, it was determined that silver nanoparticles loaded with paclitaxel increased cytotoxicity in different cancer cells.[34] In a recent study, Huang et al. demonstrated that the

colon cancer cell HT-29 may be passively targeted by the enhanced permeability and retention (EPR) effect of a lycopene nanogold nanoemulsion with an average particle size of 21.3 nm. They clarified that the reason for the anticancer effect of the generated nanostructures was their capacity to pass through the extracellular matrix and into the cytoplasm and nucleus.[35,36]

In the present study, OE and OTE-Ag NPs at a specific concentration were treated with MCF-7 cells for 48 h to evaluate their cytotoxic effect. MTT assay was used to measure the cytotoxic effects. A dose-dependent cell death response was observed for the OE and OTE-Ag NPs (Fig. 3). OE exhibited a considerable degree of cytotoxicity on MCF-7 breast cancer cells. In addition, the OTE-Ag NPs significantly increased the cytotoxicity of OE. Furthermore, it was found that MCF-7 breast cancer cells responded far better to OE and OTE-Ag NPs than normal HUVEC. In MCF-7 cells, undiluted OE (at a 1:1 ratio) killed approximately half of these cells (Fig. 3a), whereas OTE-Ag NPs at a dilution of 1:8 killed 61% of the cells (Fig. 3b). Compared to OTE-Ag NPs, which had an IC 50 of less than 1:8, OE had an IC 50 of 1:1 in MCF-7 cells. Thus, compared to OE, OTE-Ag NPs exhibited at least an eight-fold increase in cytotoxicity towards MCF-7 cells. HUVEC cells showed less cytotoxicity from OE, but at a 1:8 dilution, OTE-Ag NPs resulted in approximately 46% cell death (Figs. 3c and 3d). It is evident from the comparison of HUVEC and MCF-7 cells that OTE-Ag NPs have a more cytotoxic effect on MCF-7 cancer cells (Fig. 3).

Accordingly, the photo/ultrasound developed OTE-Ag NPs in this study improved OE's cytotoxicity and shown selectivity for MCF-7. Moreover, we found that the OTE-Ag NPs we synthesized exhibited proapototic, chemoprotective, cytotoxic and cell cycle inhibitory properties on cancer cells, considering the anticancer effects of oolong extract.

Apoptotic activity of the photo/ultrasound synthesized OTE-Ag NPs.—This study clearly shows that OTE-Ag NPs have better efficacy against MCF-7 cells than OE. Therefore, the apoptotic effect of OTE-Ag NPs on MCF-7 cells and their effect on the cell cycle were investigated in our study. The apoptotic effect of the OTE-Ag Nps was investigated using annexin/PI flow cytometry in MCF-7 cells. After 48 h of application, OTE-Ag Nps was shown to cause cell death by apoptosis in MCF-7 cells at an IC_{50} value of approximately. Untreated MCF-7 cells were 89.58% alive, 3.80% were observed as early apoptosis and 4.34% as late apoptosis. MCF-7 cells treated with OTE-Ag-Nps had a survival rate of 48.47%; however, 46.48% and 4.81% of the cells underwent early and late apoptosis, respectively (Fig. 4). Furthermore, necrotic cell death was not induced by the OTE-Ag NPs. In summary, our study demonstrated that OTE-Ag NPs induced apoptosis and inhibited the proliferation of breast cancer cells.

Cell cycle arrest of the photo/ultrasound synthesized OTE-Ag NPs.—Although chemotherapeutics induces cell damage and death, the regulation of apoptosis and the cell cycle truly govern cell death. Cell cycle checkpoints are biochemical mechanisms that block cell cycle transition or cause cell death in response to stress.[37] Cell cycle progression is continually tracked to ensure that events in the process of cell division occur correctly and to avoid the proliferation of

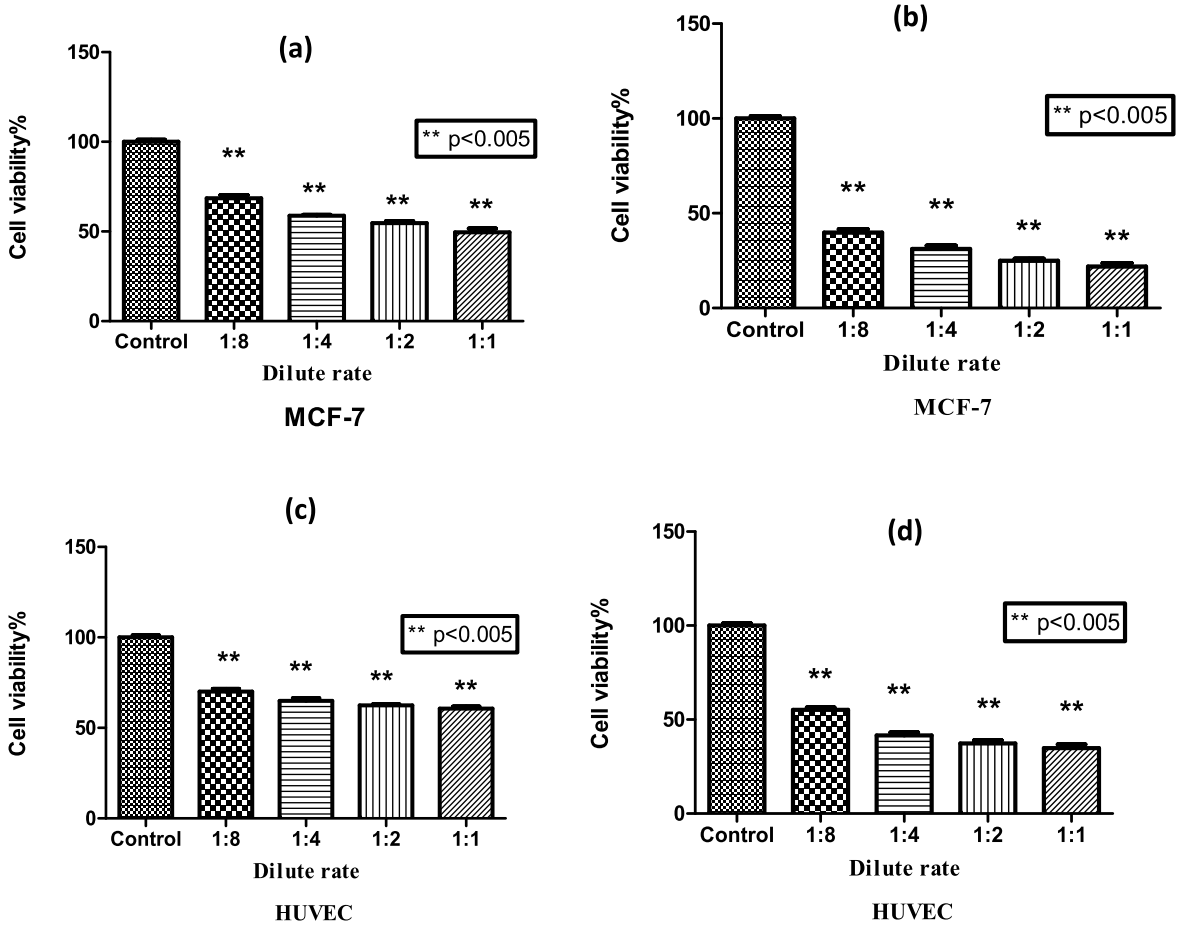

Figure 3. OE and photo/ultrasound synthesized OTE-Ag NPs' cytotoxic effects on MCF-7 and HUVEC cells. The cytotoxicity of OE (a) and OTE-Ag NPs (b) on MCF-7 cells and the effect of OE (c), and OTE-Ag NPs (d) on HUVEC cells are demonstrated. Note: OE (a) and OTE-Ag NPs (b) concentrations were administered by dilution at 1/8, 1/4, 1/2, and 1 times. P values of 0.01:** denotes statistical significance when compared to the control group. The Student's t-test was used to analyze the samples. GraphPad Prism 8.0 (GraphPad Software, San Diego, CA, USA) was used for statistical analysis. At least three attempts were made in each test.

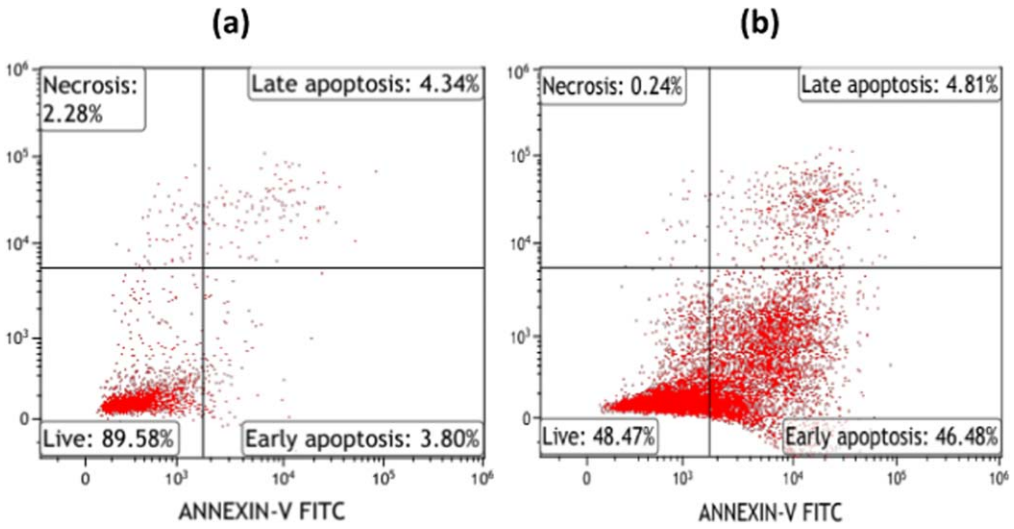

Figure 4. Apoptotic effects of OTE-Ag NPs on MCF-7 cells determined by flow cytometry Apoptosis rates in control (untreated MCF-7) (a) and OTE-Ag NPs treated MCF-7 cells (b). MCF-7 cells were incubated at approximately the IC_{50} of OTE-Ag NPs for 48 h.

DNA-damaged cells. Checkpoints for replication and DNA damage block or slow down the cell cycle transition, re-establishing the proper cell cycle sequence once the damage has been repaired. The cell was determined to die if repair was not possible. For every phase of the cell cycle, one or more checkpoints have been established.[38,39]

This study showed that OTE-Ag NPs are more effective than OE in MCF-7 cells. To this end, our study investigated the effect of OTE-Ag NPs on the cell cycle of MCF-7 cells. As shown in Fig. 4, 42.37% of MCF-7 cells in the untreated control group were in the G1/G0 phase, whereas 38.85% of MCF-7 cells treated with OTE-Ag NPs were in this phase. The S phase showed a modest increase to 18.34% in MCF-7 cells treated with OTE-Ag NPs compared to 17.73% in the control group. In the G2/M phase, the population of MCF-7 cells increased from 39.87% to 42.82% in the group treated with OTE-Ag NPs compared to that in the control group (Fig. 5). Our results showed that OTE-Ag NPs induced apoptosis in MCF-7 cells by arresting the cell cycle at the G2/M phase. According to our results, OTE-Ag NPs promote G2/M cell cycle arrest and apoptosis in MCF-7 cells.

The most common biomarker for CSCs in various cancer types is the multifunctional glycoprotein cluster of differentiation CD44, which functions as a type of receptor for hyaluronic acid (HA) along with other extracellular matrix (ECM) molecules.[40] Cancer cell migration, invasion, and motility are all related to CD44's binding to cytoskeletal proteins, which in turn promotes actin cytoskeletal remodeling.[41]

The MCF-7 cell line was treated with photo/ultrasound-produced OTE-Ag NPs at an IC 50 value in this investigation. The percentage of cells expressing the surface indication CD44+/CD24-, which is linked to highly tumorigenic breast cancer, was compared with that of the MCF-7 cell line that had not received any treatment. The association between poor prognosis and the presence of CD44+/CD24- was statistically significant according to numerous studies.[40,41] In the present study, the CD44+/CD24- ratio in the MCF-7 control cell line was 84.79%, which decreased to 47.7% in the MCF-7 cell line treated with OTE-Ag-NPs (Figs. 6c and 6d). A direct correlation between the decrease in the CD44+ ratio in these cells and the induction of apoptosis by MCF-7 cells treated with the photo/ultrasound synthesized OTE-Ag NPs was also observed.

Cluster of differentiation CD44 is the most widely used marker of CSCs, and expression of CD44 has been associated with resistance to anticancer medications, metastasis, and tumor recurrence.[40]

Numerous studies have suggested that oolong tea has anticancer effects; however, in this study, we demonstrated that silver-bound green photo/ultrasound-developed OTE-Ag NPs enhanced the anti-proliferative effect in cancer cells. In addition, as markers of anticancer action, the OTE-Ag-NPs demonstrated substantial activation of apoptosis and cell cycle arrest in the G2/M phase. Additionally, it was shown that NPs have high selectivity and sensitivity for H_2O_2 detection.

Digital H_2O_2 biosensor utilizing the OTE-Ag NPs.—It is critical to develop novel techniques with high selectivity and sensitivity for measuring H_2O_2 in vivo or in vitro. Tumor cells generate more H_2O_2 than normal cells because of their rapid proliferation; this may be exploited as an effective target to identify normal tissues and build distinct diagnostic and therapeutic strategies.[42–44]

The photo/ultrasound synthesized OTE-Ag NPs-based biosensor was used in this study, opting for a digital colorimetric approach for the detection of H_2O_2. The obtained results were evaluated using color channels, and subsequently, the value of each sample image was determined using the red-green-blue (RGB) color strategy. In this digital colorimetric approach, each color is represented by a number ranging from zero to 255. To demonstrate the interaction of the OTE-Ag NPs-based biosensor and the target analyte (H_2O_2), we performed a detailed investigation using a non-enzymatic digital sensor strategy. Using ImageJ software, we analyzed the color change during the digital colorimetric oxidation/reduction process of electroactive compounds using photographic pixels of samples dropped on filter paper and dried.

In this study, samples with a circular diameter of 1.5 cm × 1.5 cm were detected on Whatman® qualitative filter paper. The target analytes (200 µl) were dropped onto filter paper and dried in a vacuum oven at 37 °C. Photographs of the prepared sensors were taken at a distance of 20 cm using a smartphone.

The digital photographs of the OTE-Ag NPs-based biosensor were given in Fig. 6. These included: (a) paper-biosensor in 100 µM of various analytes (glucose, lactose, maltose, testosterone, dopamine, and progesterone) (b) paper-biosensor in a concentration range of 0.5–100 µM of H_2O_2; (c) plot of Log C–S (%); (d) plot of Log C–ΔE, and (e) biosensor's selectivity analysis. The prepared OTE-Ag NPs-based biosensor's response (S), Euclidean distance (ΔE), LOD, and LOQ values were calculated for the H2O2 digital sensing platform, which is sensitive and selective, using Eqs. 2–4.[45,46]

$$\Delta E = \sqrt{(R_i - R_0)^2 + (G_i - G_0)^2 + (B_i - B_0)^2} \quad [2a]$$

$$S = 100\frac{x_c - x_0}{x_0 - x_{ref}}[\%] \quad [3a]$$

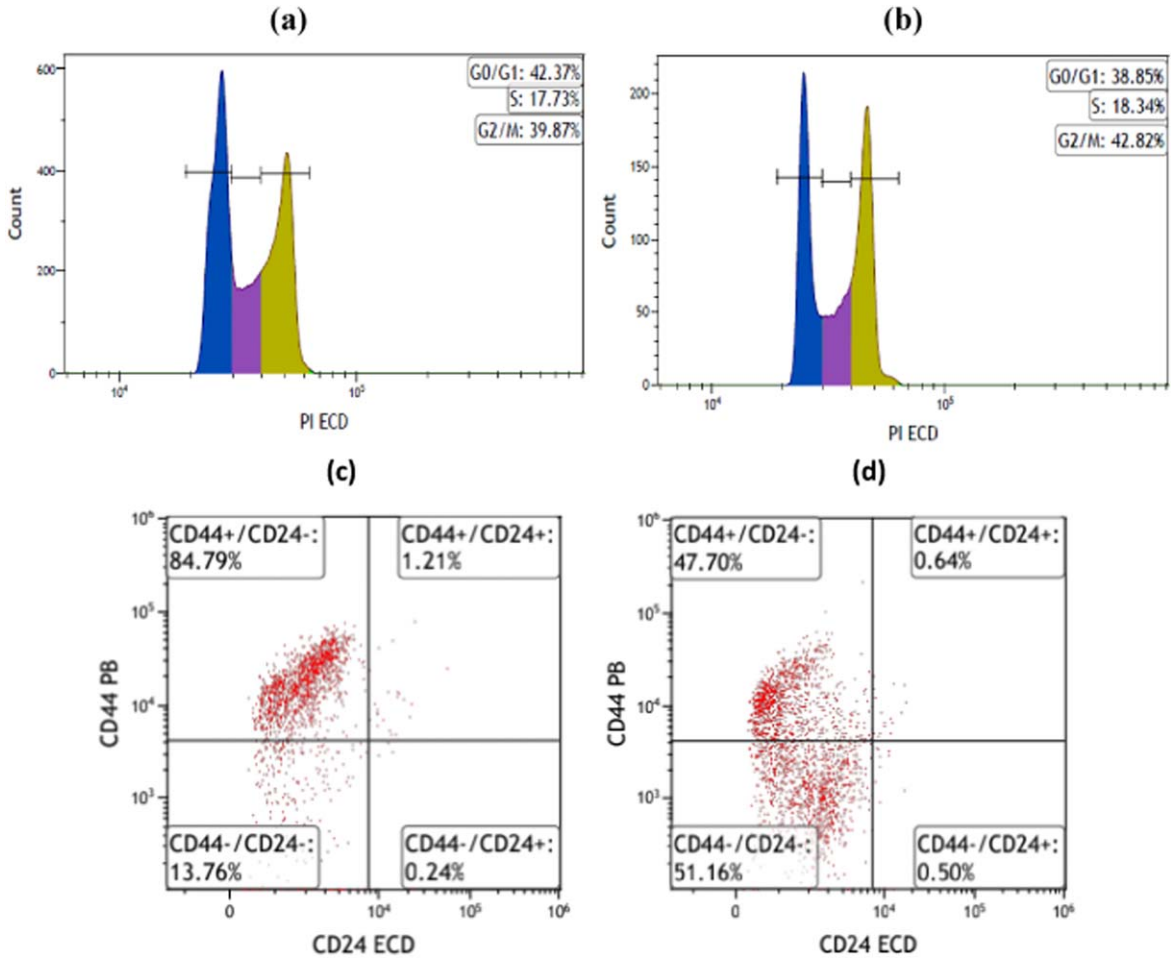

Figure 5. Flow cytometric analysis of cell cycle arrest in MCF-7 cells. MCF-7 cells were incubated at the approximate IC 50 of OTE-Ag NPs for 48 h. Using a flow cytometer, (a) Cell cycle diagram in untreated MCF-7 cells (b) Cell cycle diagram in MCF-7 cell line treated with OTE-Ag NPs was shown. CD44+/CD24 ratios in (c) untreated MCF-7 cells and (d) MCF-7 cell line treated with OTE-Ag NPs, also by flow cytometry.

$$S(\%) = mLog(C) + n \quad [4a]$$

$$LOD = 3.3\sigma/m \quad [5]$$

$$LOQ = 10\sigma/m \quad [6]$$

Gi and Go: Green value of the sample and the blank paper, Ri and Ro:Red value of the sample and blank paper, Bi and Bo:Blue value of the sample and blank paper, xc: Blue value of the sample, xo: Blue value of the sensor, xref: Blue value of the blank, S: Response, and σ: The standard deviation.

Specifically, the impact of various substances (including glucose, lactose, maltose, testosterone, dopamine, and progesterone) on the detection of H_2O_2 was investigated as well. The sensitive and selective properties of the photo/ultrasound synthesized OTE-Ag NPs-based biosensor were employed with the simple Image J software. When other analytes, such as glucose, lactose, maltose, testosterone, dopamine, and progesterone, were present, we did not see no color change was observed (Fig. 6a), but the detection showed that H_2O_2 underwent an obvious color shift. The color of the sample changed from brown to ivory color after one minute, utilizing an H_2O_2 range of 0.5–100 μM (Fig. 6b). The prepared biosensor demonstrated highly selective efficiency with a LOD of 0.102 μM and LOQ of 0.310 μM in a range of 0.5–100 μM, referring to the digital colorimetric results of OTE-Ag NPs-based biosensor (Fig. 6c). Additionally, a broad range of 0.5–100 μM was found when the ΔE values of the OTE-Ag NPs-based biosensor were colorimetrically altered, increasing from 12.23 to 309.33 (Fig. 6d). The RGB results showed that the OTE-Ag NPs-based biosensor's ΔE values for (glucose, lactose, maltose, testosterone, dopamine, progesterone, and H_2O_2 were 1.65, 7.43, 9.73, 12.21, 30.15, 64.32, and 309.33, respectively (Fig. 6e). Table II presents a comparative analysis of the sensing performance of previously developed sensors for measuring H_2O_2.

Table II presents a comprehensive comparison of the sensors developed for H_2O_2 measurements. Notably, the novel photo/ultrasound synthesized OTE-Ag NPs-biosensor in this study stands out for its exceptional features, including a low LOD of 0.102 μM and a spherical morphology with a particle diameter ranging from 10 to 20 nm.

Electrochemical and machine learning based analysis.—In this section, electrochemical and ML-based analyses are presented, where the LOD for urea and fructose was computed using CV data. This analysis was aimed at enhancing the precision and dependability of the biosensor, with LOD values determined to be 3.02 μM for urea and 4.86 μM for fructose. CV responses of each analyte are shown in Fig. 7.

Next, the application of ML techniques to enhance the analysis of CV data was explored. A detailed feature-engineering process was initially performed. Key features were extracted from the CV data to capture the critical aspects of the electrochemical behavior. These included:

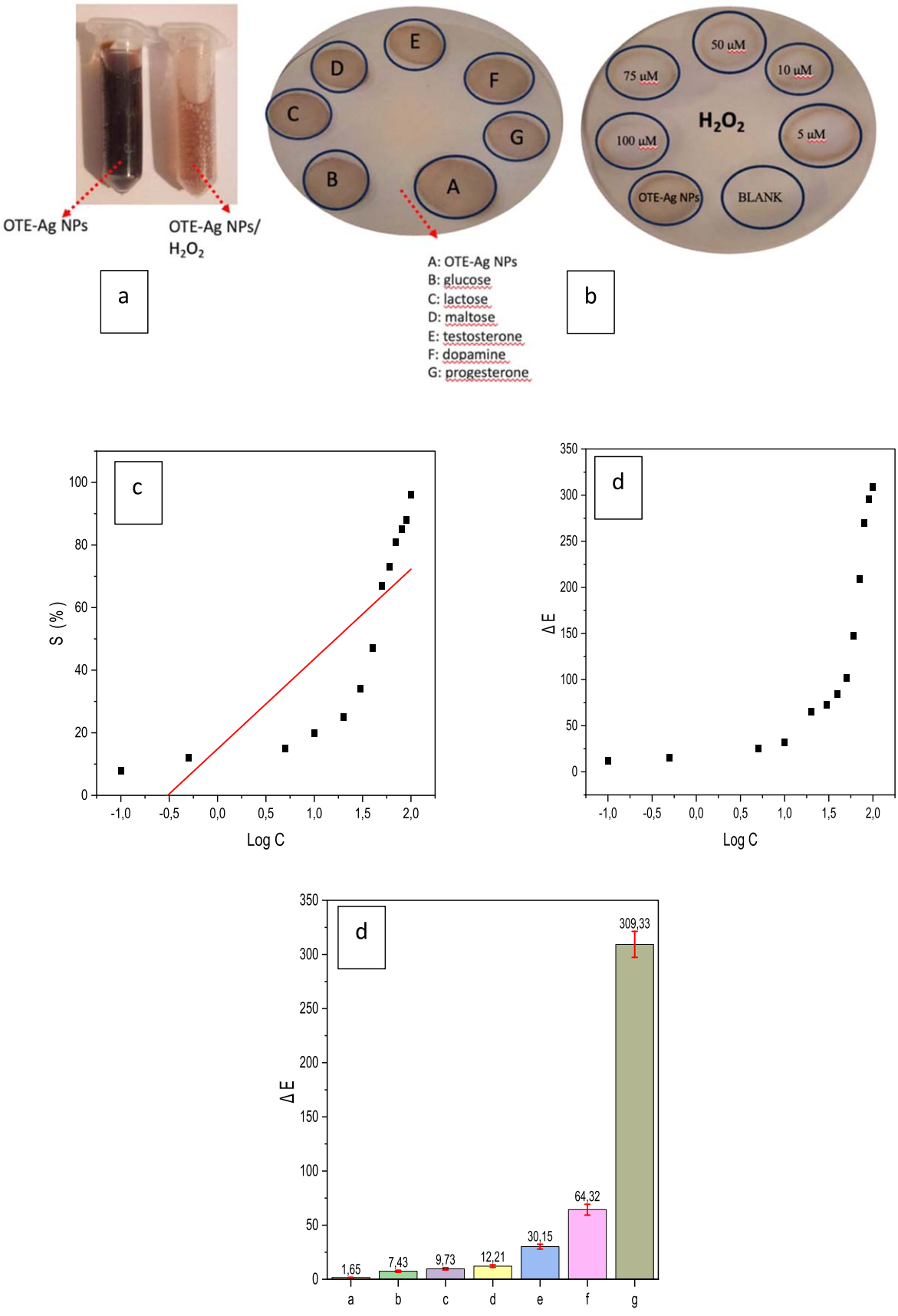

Figure 6. Digital photographs of the photo/ultrasound synthesized OTE-Ag NPs-based biosensor, showcasing: (a) the paper-biosensor in 100 µM of various analytes (glucose, lactose, maltose, testosterone, dopamine, and progesterone); (b) the paper-biosensor in a concentration range of 0.5–100 µM of H_2O_2; (c) the plot of Log C–S (%); (d) the plot of Log C–ΔE; and (e) the biosensor's selectivity measurements.

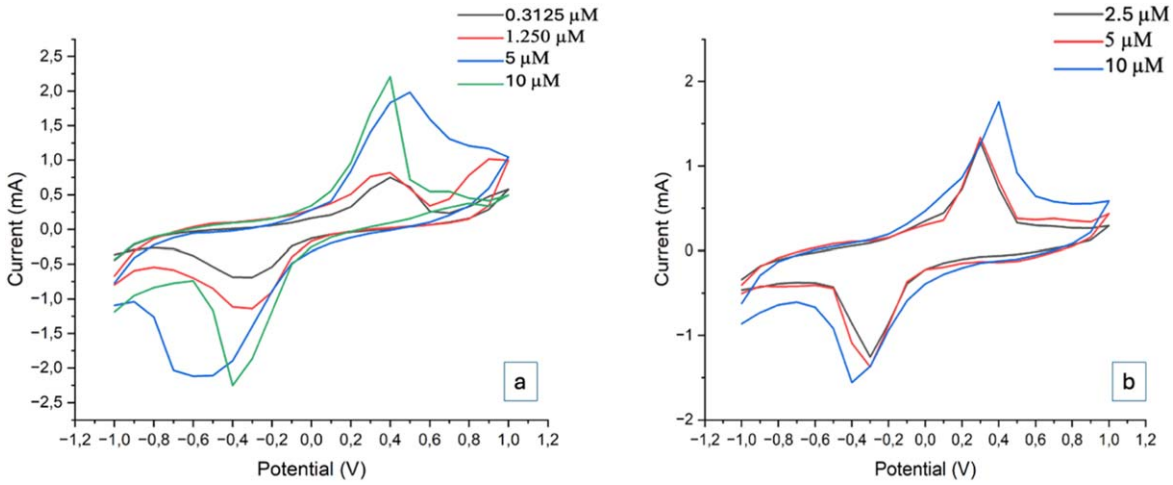

Figure 7. The CV responses comparing the anodic/cathodic peak current and potential for OTE-Ag NPs concerning (a) urea and (b) fructose.

Table II. Comparison of the sensing capacities of previously developed sensors for measuring H_2O_2.

Nanomaterials	Characterization	Results	References
Ag NPs immobilized on FeS_2 nanoprisms	Hexagonal rod crystals: 2 μm length, 500 nm gyration diameter.	LOD (colorimetric): 3.0 μM. LOD (electrochemical): 0.6 μM.	47
Apple juice extract-based Ag NPs	Spherical shape, 60 nm diameter, particle size ranges from 6 to 100 nm.	LOD: 0.2656 ppm	48
Ag–Ti_3C_2 nanohybrids	10–140 nm in diameter	LOD: 0.31 μM	49
Ag NPs/halloysite nanotubes	tubular morphology	LOD: 0.7 μM	50
Mangifera indica leaves extract-based Ag NPs	particle size of 22 nm	LOD: <60 μg l^{-1}	51
Cinnamon extract-based Ag NPs	particle sizes ranging from 10 to 70 nm	LOD: 0.48 μM	52
OTE-Ag NPs	particle diameter ranging from 10 to 20 nm	Digital LOD: 0.102 μM (H_2O_2) and ML-based electrochemical LOD: 3.02 μM (urea) and 4.86 μM (fructose)	In this study

- **Charge (Q)**: Total electric charge passed during the electrochemical reaction.
- **Half-Peak Potential**: The potential at which the current is half its peak value.
- **Peak Width at Half Height**: Measures the width of the peak at half its maximum height, indicating sharpness.
- **Current Statistics**: Including mean current, median current, and standard deviation, which describe the central tendency and variability of the current.
- **Higher-Order Current Derivatives**: Both Peak Derivative and Peak Second Derivative were calculated to identify rapid changes in the reaction kinetics.
- **Kurtosis and Skewness**: These statistical measures describe the shape and asymmetry of the current distribution.
- **Peak Currents and Potentials**: Positive and Negative Peak Currents and their corresponding Potentials were noted, highlighting maximum and minimum response points.

Correlation analysis was conducted to assess the relationships between each feature and the analyte concentration. This analysis was crucial for identifying features with significant correlations, either positive or negative, with the target variable. The results of this analysis are detailed in Table III.

Features demonstrating strong correlations, as shown in Table III, were subjected to further analysis using feature importance evaluation. Feature importance analysis was conducted using a Random Forest algorithm to further refine the selection of features based on their predictive power for estimating urea and fructose concentrations. This method assesses how effectively each feature contributes to the accuracy of the model and quantifies the significance of each feature in enhancing the predictive performance.

A threshold of 0.8 was set for selecting significant features, ensuring that only those with the most substantial impact on the model were retained. This threshold was strategically chosen to balance the complexity and accuracy of the model effectively. Features that surpassed this threshold were considered critical for accurate predictions because of their substantial influence on model outcomes.

From the analysis, the following features were identified as most important: **Peak Derivative**, **Peak Second Derivative, Skewness, Negative Peak Current**, **Negative Peak Potential.**

These features were selected for their significant contribution to the model's ability to accurately predict analyte concentrations based on CV data. This selection aids in constructing a more efficient and interpretable model, ensuring optimal performance while avoiding overfitting with redundant or less informative variables.

Following feature importance analysis, two distinct models - a linear regression baseline and an artificial neural network (ANN) - were developed and evaluated to predict the concentrations of urea and fructose. The ANN was implemented as a sequential feedforward network using TensorFlow/Keras. The hyperparameters of the artificial neural network were systematically optimized using Keras Tuner's RandomSearch algorithm. The hyperparameter space was extensively explored through a randomized search strategy with 10 independent trials, where each trial was executed 3 times to ensure the stability and reproducibility of results. The network architecture hyperparameters were explored within chosen ranges. For the input layer, the number of units was varied between 32 and 512, with a

Table III. Correlation coefficients between CV features and concentrations of urea and fructose.

Feature	Correlation with concentration (Urea)	Correlation with concentration (fructose)
Charge (Q)	0.635	0.993
Half-Peak Potential	−0.296	—
Peak Width at Half Height	−0.900	—
Mean Current	−0.716	−0.744
Median Current	0.539	−0.904
Standard Deviation	0.699	0.987
Kurtosis	0.898	−0.979
Skewness	−0.617	0.634
Peak Derivative	0.935	0.041
Peak Second Derivative	0.941	−0.581
Positive Peak Current	0.937	0.973
Positive Peak Potential	−0.433	0.945
Negative Peak Current	−0.908	−0.998
Negative Peak Potential	−0.452	−0.945

step size of 32. The number of hidden layers was treated as a hyperparameter and was varied between 1 and 5 layers. For each hidden layer, the number of units was also optimized within the same range as the input layer (32 to 512 units, with a step size of 32). The learning process was controlled by several key hyperparameters. The learning rate was sampled from a log-uniform distribution ranging from 10^-4 to 10^-2. This logarithmic sampling ensures thorough exploration of both fine-grained learning rates for precise optimization and larger learning rates for faster convergence. Each model configuration was trained for 200 epochs, providing sufficient time for convergence while managing computational resources. The optimization process used validation loss (mean squared error) as the objective function. After completing all trials, the best hyperparameter set was identified based on the lowest validation loss achieved across all configurations and repetitions. Following the hyperparameter optimization, the final model was constructed using the best-performing configuration:

- Input layer: 32 neurons with ReLU activation were utilized
- First hidden layer: 128 neurons with ReLU activation were implemented
- Second hidden layer: 32 neurons with ReLU activation were employed
- Output layer: 1 neuron (linear activation) for regression output was incorporated

The model was compiled using the Adam optimizer with a learning rate of 0.002, and mean squared error loss function was selected. Training was conducted for 500 epochs with a batch size of 32. Due to the limited dataset size, Leave-One-Out Cross-Validation (LOOCV) was employed to maximize the use of available data, and robust performance estimation was ensured. Features were normalized using MinMaxScaler before model training was initiated. For comparison, a linear regression model was implemented using scikit-learn's LinearRegression class, and evaluation was also performed using LOOCV. The prediction accuracy of each model was quantitatively assessed using multiple complementary metrics:

- Root Mean Square Error (RMSE): by which the standard deviation of prediction errors was measured
- Mean Absolute Error (MAE): through which the average magnitude of errors was quantified
- Coefficient of Determination (R^2): whereby the proportion of variance explained by the model was indicated

The performance metrics for each algorithm differentiated by the analyte are summarized in Table IV.

All experiments are run on a 24-core, 4.2 GHz desktop computer with 64 GB of RAM. As shown in Table IV, the ANN showed strong prediction results for urea. Although the performance for fructose was robust, it was slightly lower than that of urea, indicating differences in the signal characteristics between the two analytes. The ANN model provided accurate and reliable predictions for both urea and fructose concentrations with notably better results for urea. This superior performance could be attributed to the ANN's capability to effectively learn nonlinear and complex dependencies between variables, which are prevalent in electrochemical data analyzed by CV.

Table IV. Prediction performance of ML algorithms.

Model	Analyte	RMSE	MAE	R^2
Linear Regression	Urea	2.9221	1.8568	0.5820
	Fructose	1.3246	1.2606	0.8195
ANN	Urea	0.4266	0.3380	0.8575
	Fructose	0.4832	0.3806	0.8252

These results underline the potential of using advanced ML techniques to enhance the predictive accuracy of models in chemical analysis, especially in electrochemical sensing. Given its robust performance across both analytes, the ANN model is recommended as the preferred method for similar predictive tasks within this field.

This comparative analysis highlights the importance of selecting an appropriate MLmodel based on specific dataset characteristics and analysis objectives, demonstrating the varying capabilities of different approaches when applied to complex chemical data.

Conclusions

In conclusion, this study investigated the frontiers of cancer treatment, with a particular emphasis on the development of multifunctional nanoplatforms with anticancer capacities and the rapid and precise detection of putative cancer biomarkers for early diagnosis. The production of the photo/ultrasound synthesized OTE-Ag NPs has made it possible to assess anticancer activity against MCF-7 cells and evaluate H_2O_2 via a smartphone image strategy. Our digital sensor studies underscored the remarkable sensitivity and selectivity of OTE-Ag NPs in detecting H_2O_2, achieving exceptional colorimetric sensor values within a mere minute. The H_2O_2 sensor consistently demonstrated a low LOD of 0.102 μM across the range of 0.5–100 μM, as evidenced by the digital colorimetric results. Moreover, the application of ML techniques significantly enhanced the predictive accuracy of analyte concentrations using CV data. The feature engineering process, coupled with feature importance analysis, enabled the selection of the most predictive features, resulting in robust models. The ANN model demonstrated strong predictive performance, especially for

urea concentrations. The integration of ML in this study highlights the potential of these advanced techniques to improve the precision and reliability of chemical analysis in electrochemical sensing. This study has limitations, including the single-use nature of the ML based sensors, which may hinder long-term monitoring. Potential green matrix effects in complex bio-based samples and the need for further validation in real-world conditions should also be considered. While the biosensors showed good selectivity against common interferents, additional studies are needed to assess their robustness in diverse biological contexts. Future work could focus on developing reusable sensor designs, using more stable nanostructures, or integrating hybrid electrochemical and optical platforms to improve performance and broaden the range of detectable analytes. Overall, this work provides a promising biosensing strategy, but further research is needed to optimize sensor capacity, performance and explore broader biomedical applications.

Our investigations into cytotoxicity, apoptosis, cell cycle arrest, and the expression of the CD44 surface marker unveiled the selective harm inflicted by OTE-Ag NPs on MCF-7 cells. The MTT assay was used to carefully evaluate the cytotoxic effects, and the results showed that OTE-Ag NPs could inhibit MCF-7 cell proliferation while showing less cytotoxicity in normal HUVEC cells. Moreover, the apoptotic impact demonstrated the capacity of OTE-Ag NPs to induce apoptosis and was ascertained by flow cytometry analysis with Annexin V/PI dye. Notably, MCF-7 cells were arrested by OTE-Ag NPs in the G2/M phase, providing information regarding their regulatory effects on the cell cycle. When OTE-Ag NPs were applied to MCF-7 cells, the expression of CD44, a marker for CSCs, was significantly lower than in untreated cells. This finding suggests that OTE-Ag NPs may play a role in inhibiting metastasis. To summarize, our research highlights the noteworthy restraint of OTE-Ag NPs on MCF-7 cell growth, mainly via the apoptotic route by controlling the cell cycle at the G2/M stage. Furthermore, the reduction in CD44 expression that has been seen increases the possibility that the photo/ultrasound synthesized OTE-Ag NPs can inhibit metastasis, making them attractive candidates for additional research into cancer therapies.

ORCID

Fatih Özbaş https://orcid.org/0000-0002-6655-9363
Selcan Karakuş https://orcid.org/0000-0002-8368-4609

References

1. S. Wang et al., *Food Science and Human Wellness*, **11**, 512 (2022), https://researchgate.net/publication/363127904_Multifunctional_health-promoting_effects_of_oolong_tea_and_its_products.
2. H. Shi, J. Liu, Y. Tu, C. E. Freter, and C. Huang, *Anticancer Res.*, **38**, 6217 (2018), https://pubmed.ncbi.nlm.nih.gov/30396940/.
3. A. A. Mailk, K. A. Wani, and S. R. Ahmad, *JMS SKIMS*, **15**, 7 (2012), https://uzv.jmsskims.org/index.php/jms/article/view/103.
4. D. Y. Lim and B. H. Hwang, *Biotechnol. J.*, **19**, 2300156 (2024).
5. A. Q. Figueiredo, C. F. Rodrigues, N. Fernandes, I. J. Correia, and A. F. Moreira, *Biotechnol. J.*, **19**, 2300019 (2024).
6. S. Jeyarani et al., *J. Photochem. Photobiol., B*, **202**, 111715 (2020).
7. D. A. Fernandes et al., *J. Photochem. Photobiol., B*, **218**, 112110 (2021).
8. S. Rawal and M. M. Patel, *Journal of Controlled Release*, **301**, 76 (2019).
9. W. Yan, Y. Chen, Y. Yao, H. Zhang, and T. Wang, *Cancer Cell Int.*, **13**, 1 (2013).
10. M. Al-Hajj, M. S. Wicha, A. Benito-Hernandez, S. J. Morrison, and M. F. Clarke, *Proc. Natl. Acad Sci. U S A*, **100**, 3983 (2003).
11. N. P. Shetti, D. S. Nayak, S. J. Malode, and R. M. Kulkarni, *J. Electrochem. Soc.*, **164**, B3036 (2017).
12. M. Farrell, W. Hawley, R. Reaume, A. Gurrola, and A. K. Pradhan, *J. Electrochem. Soc.*, **164**, B3008 (2017).
13. J. Zhang et al., *J. Electrochem. Soc.*, **164**, B3001 (2017).
14. Y. Ma et al., *Food Chem.*, **429**, 136850 (2023).
15. R. Thirunavukarasu, G. P. Doss C, G. R, M. Gopikrishnan, and V. Palanisamy, *Comput. Biol. Med.*, **149**, 106020 (2022).
16. C. Mosquera-Lopez, K. L. Ramsey, V. Roquemen-Echeverri, and P. G. Jacobs, *Comput. Biol. Med.*, **155**, 106670 (2023).
17. E. Longato et al., *Comput. Biol. Med.*, **96**, 141 (2018).
18. F. Cui, Y. Yue, Y. Zhang, Z. Zhang, and H. S. Zhou, *ACS Sens.*, **5**, 3346 (2020).
19. N. Ha, K. Xu, G. Ren, A. Mitchell, and J. Z. Ou, *Advanced Intelligent Systems*, **2**, 2000063 (2020).
20. L. C. Crowley, B. J. Marfell, A. P. Scott, and N. J. Waterhouse, *Cold Spring Harb Protoc*, **2016**, 953 (2016), https://pubmed.ncbi.nlm.nih.gov/27803250/.
21. E. Karakus¸a et al., *J. Drug Deliv. Sci. Technol.*, **94**, 1773 (2024).
22. L. Huang, X. Weng, Z. Chen, M. Megharaj, and R. Naidu, *Spectrochimica Acta Part A: Molecular and Biomolecular Spectroscopy*, **117**, 801 (2013).
23. M. Amin, T. Safa, and H. Koohestani, *Results in Engineering*, **21**, 101808 (2024).
24. E. Z. Okka et al., *Optik*, **294**, 171487 (2023).
25. J. Wang, W. Liu, Z. Chen, and H. Chen, *Biomedicine & Pharmacotherapy*, **90**, 160 (2017).
26. M. Sherjeel et al., *Int. J. Biol. Macromol.*, **257**, 128544 (2024).
27. K. Shameli et al., *Int. J. Nanomedicine*, **7**, 5603 (2012), https://dovepress.com/green-biosynthesis-of-silver-nanoparticles-using-curcuma-longa-tuber-p-peer-reviewed-fulltext-article-IJN.
28. S. Sharmin et al., *Heliyon*, **9**, 2405 (2023).
29. J. He et al., *Inorg. Chem. Commun.*, **160**, 112021 (2024).
30. P. Batra and A. K. Sharma, *3 Biotech*, **3**, 439 (2013), /pmc/articles/PMC3824783/.
31. M. K. Chahar, N. Sharma, M. P. Dobhal, and Y. C. Joshi, *Pharmacogn. Rev.*, **5**, 1 (2011), /pmc/articles/PMC3210013/.
32. B. Pannerselvam et al., *Processes*, **9**, 888 (2021), https://mdpi.com/2227-9717/9/5/888/htm.
33. A. W. Alshameri and M. Owais, *Open Nano*, **8**, 100077 (2022).
34. F. Danışman-Kalındemirtaş, A. Karİper, C. Hepokur, and S. Erdem-Kuruca, *J. Drug Deliv Sci. Technol.*, **61**, 102265 (2021).
35. Y-H. Lin et al., *Molecules*, **26**, 3260 (2021), https://mdpi.com/1420-3049/26/11/3260/htm.
36. R. F. S. Huang, Y. J. Wei, B. S. Inbaraj, and B. H. Chen, *Int. J. Nanomedicine*, **10**, 2823 (2015).
37. J. A. Pietenpol and Z. A. Stewart, *Toxicology*, **181–182**, 475 (2002).
38. G. Damia and M. Broggini, (2003), https://tandfonline.com/action/journalInformation?journalCode=kccy20http://landesbioscience.com/journals/c.c./tocnew31.php?volume=3&Issue=1.
39. M. H. Lam, Q. Liu, S. J. Elledge, and J. M. Rosen, *Cancer Cell*, **6**, 45 (2004), https://europepmc.org/article/med/15261141.
40. I. geun Ryoo, B. hyun Choi, S. K. Ku, and M. K. Kwak, *Redox Biol.*, **17**, 246 (2018), https://cuk.elsevierpure.com/en/publications/high-cd44-expression-mediates-p62-associated-nfe2l2nrf2-activatio.
41. S. Tsukita et al., *J. Cell Biol.*, **126**, 391 (1994), https://pubmed.ncbi.nlm.nih.gov/7518464/.
42. Z. Chu et al., *Coord. Chem. Rev.*, **481**, 215049 (2023).
43. F. Gao et al., *Colloids Surf. B Biointerfaces*, **82**, 359 (2011), https://pubmed.ncbi.nlm.nih.gov/20889315/.
44. S. E. Salamifar, S. Lee, and R. Y. Lai, *Colloids Surf. B Biointerfaces*, **123**, 866 (2014).
45. L. Engel et al., *Sens. Actuators B Chem.*, **330**, 129281 (2021).
46. A. G. Ayankojo, J. Reut, V. Ciocan, A. Öpik, and V. Syritski, *Talanta*, **209**, 120502 (2020).
47. D. Li, R. Tian, S. Kang, X.-Q. Chu, D. Ge, and X. Chen, *Food Chemistry*, **393**, 133386 (2022).
48. K. S. Kumar and T. Ramakrishnappa, *J. Environ. Chem. Eng.*, **9**, 105365 (2021).
49. P. Jin, W. Tan, X. Li, J. Fan, and K. Li, *Talanta*, **260**, 124619 (2023).
50. X. Zhu et al., *Applied Clay Science*, **242**, 107022 (2023).
51. N. D. Hai et al., *Diam. Relat. Mater.*, **138**, 110264 (2023).
52. A. Elgamouz et al., *Colloids Surf. A Physicochem Eng. Asp.*, **647**, 129035 (2022).